

NPR effect on energy absorption enhancement of star-shaped honeycomb filled shear thickening fluids under impact

J.P. Ren^{a,b,1}, Z.P. Gu^{a,1}, Y.D. Sui^{a,c}, A.G. Zhao^{b,*}, C.G. Huang^{a,c}, X.Q. Wu^{a,c,**}

^a Key Laboratory of Mechanics in Fluid Solid Coupling Systems, Institute of Mechanics, Chinese Academy of Sciences, Beijing, 100190, China

^b College of Civil Engineering, Nanjing Tech University, Nanjing, 211816, China

^c School of Engineering Science, University of Chinese Academy of Sciences, Beijing, 100049, China

ARTICLE INFO

Handling Editor: Prof. Ole Thomsen

Keywords:

Shear thickening fluid
Star-shaped honeycombs
Negative Poisson's ratio
Dynamic energy absorption behavior
Critical impact velocities

ABSTRACT

Porous materials filled with shear thickening fluids (STF) can adapt flexibly to complex dynamic loadings environments, showing great promise as an advanced composite material with high impact resistance. However, the energy absorption performance of these STF related materials is not fully exploited due to the low coupling efficiency between the STF and the structure. In this paper, the dynamic compressive behavior of STF filled star-shaped honeycombs (SSH) with significant negative Poisson's ratio (NPR) effect was studied using modified SHPB experiments and finite element (FE) simulations. The coupling mechanism between the NPR effect and the shear-thickening behavior of STF is analyzed. The dynamic mechanical performance of the STF-filled SSH (SSH-STF) under initial velocity impact and constant velocity compression loading, including stress distribution, energy dissipation, and coupling strength, is comprehensively analyzed. The results indicate that SSH-STF enhances energy absorption efficiency by the mutual extrusion effect of SSH and STF, which limits local deformation and modifies the unstable deformation mode of SSH, while also expanding the energy absorption region. The shear thickening effect of STF limits 82 % of the in-plane rotation behavior of SSH-STF unit cells compared to unfilled SSH under high-velocity impact, promoting uniform and sufficient contraction deformation across the unit cells, which enhances the mean crushing force by 253 %. Meanwhile, the shear thickening behavior of STF leads to faster stress transfer within SSH, significant enhancement of the local deformation stability and effectively increasing the critical impact velocity of the SSH-STF. In this paper, the significant enhancement of energy absorption performance of the STF-SSH composite provides valuable insights for the design of STF-filled auxetic honeycomb structures in practical applications.

1. Introduction

Auxetic honeycomb metamaterials have attracted considerable attention in recent years due to their lightweight, high specific strength, and flexible design capabilities, which have been widely used in impact protection fields such as automotive and aerospace [1,2]. The auxetic honeycombs can promote overall deformation through compression and contraction, enhancing energy absorption performance compared to traditional honeycombs [3–5]. Although numerous studies have focused on optimizing designs to improve energy absorption [6–10], the plastic

hinge mechanism and high porosity of the auxetic honeycomb structures have seemingly led to a bottleneck in further enhancement [10,11].

Stiffness and energy absorption capacity of auxetic honeycomb structures can be enhanced by filling different kinds of materials [12–17]. Generally, filling with soft materials such as polyurethane foam, which undergo densification earlier during compression, can delay the buckling of cell walls of auxetic honeycomb, effectively increasing its resistance to localized impact [10,18]. In addition, the failure mode transition of auxetic honeycombs filled with soft materials from interlayer failure to localized shear band failure can increases the

* Corresponding author.

** Corresponding author. Key Laboratory of Mechanics in Fluid Solid Coupling Systems, Institute of Mechanics, Chinese Academy of Sciences, Beijing, 100190, China.

E-mail addresses: shiang.37@163.com (A.G. Zhao), wuxianqian@imech.ac.cn (X.Q. Wu).

¹ These authors contributed equally to this work.

energy-absorbing region of the structure [14]. In contrast, filling auxetic honeycombs with rigid materials increases the stiffness. The extrusion and friction interactions during compression provide superior energy absorption performance [15,16]. It can be seen that the filling of soft materials primarily optimizes the deformation mode of auxetic honeycomb structures, and the energy absorption still dominated by the plastic deformation of the honeycomb itself, which limits the energy absorption capacity [12,19]. The harder fillers can increase energy absorption by increasing stiffness during compression. However, the overall deformation is generally restrained due to the localized failure under initial impact loading in honeycombs [13,16,20]. Therefore, some intelligent filler materials, which can rapidly enhance the overall deformation response during the initial stage of impact loads and then increase the structural stiffness during continued deformation, are required for auxetic honeycomb structures to enhance the energy absorption capacity.

Shear thickening (ST) [21–23] materials that show transition from soft to rigid under loading are primarily classified into shear thickening fluids (STF) [24–28] and shear thickening gels (STG) [29–31]. STGs are widely applied in personal protective materials due to their excellent energy dissipation and sealing advantages. [32,33]. Liao et al. [32] developed a novel hybrid auxetic foam by filling auxetic polyurethane foam (APF) with STG, demonstrating significant impact force attenuation along with notable self-healing capabilities. Sun et al. [34,35] explored the impact resistance of honeycombs filled with STG and observed that STG reduced significantly the structural penetration depth and impact damage severity. Furthermore, Li et al. [29,36] demonstrated that partial filling of zero Poisson's ratio metamaterials with STG enhanced energy absorption efficiency by 85 % under low-velocity impacts. Notably, the study by Gong et al. [37,38] showed that shear stiffening gel (SSG) transforms from a plastic to a rubbery state and then to a glassy state under loading, demonstrating application potential similar to STG in personal protection. By integrating SSG with Kevlar, Gong et al. [39] developed successfully multifunctional body armor with a 353 % improvement in impact force attenuation. Wu et al. [40–42] revealed that the NPR effect enhances significantly the coupling behavior between the NPR skeleton and SSG, increasing the energy absorption rate (EAR) by 76.3 % under low-velocity impact.

Notably, the viscosity of STF increases significantly at the critical shear strain, enabling its effective application in impact protection engineering [43–48]. Wu et al. [49,50] fabricated successfully STF microcapsules with significant shock attenuation capability. Lu et al. [51, 52] observed that the STF composite structure reduces the peak load by up to 154.7 % under low-velocity impact by dispersing the impact stress and creating low-stress regions. Hu et al. [53–55] elucidated the energy absorption mechanism of traditional honeycombs coupled with STF and observed that SEA decreased due to the compression-expansion behavior, which was improved by using auxetic lattice structures. However, the coupling mechanisms between auxetic honeycombs and STF under different critical impact velocity remain unclear.

In this paper, star-shaped honeycombs (SSH), which show significant NPR effect and stable deformation mode under dynamic impact loading [56–59], are chosen to explore the energy absorption potential of STF-filled SSH structures. Through modified SHPB experiments, we demonstrate the enhanced energy absorption performance of SSH-STF, while numerical simulations systematically reveal its energy enhancing coupling mechanism. SSH-STF demonstrates intelligent adaptation to loading rates and enhances energy absorption efficiency, while the coupling mechanism between STF and SSH reveals that the NPR effect and the shear thickening interaction work together to improve the overall structural response and energy absorption capacity under dynamic impact. The paper provides a new strategy for designing lightweight structures with excellent dynamic energy absorption performance in impact protection applications, such as the anti-collision structures employed in vehicles. The paper is structured as follows. Section 2 introduces the SHPB testing and finite element (FE) methods

and tests the mechanical properties of SSH and STF. Section 3 compares and validates the superior deformation mode and energy absorption behavior of SSH-STF over SSH under dynamic impact. Section 4 demonstrates the coupling mechanism between STF and SSH through shear strain rate maps, unit cell deformation, and stress transfer analysis at dynamic impact loading.

2. Materials and methods

2.1. Manufacturing of SSH structure

The SSH structure used in this study is shown in Fig. 1(a), manufactured from 6061-T6 aluminum alloy using 3D printing technology. The overall height (H) and width (L) of the SSH are both 50 mm, with the out-of-plane thickness of the cell (B) being 40 mm, and the structure is composed of a 5×5 grid of star-shaped cells. The geometry of the typical star-shaped cell, highlighted in the red dashed box, is shown in Fig. 1(b). The length of the horizontal and vertical ribs, L_a connecting to the other cells are 3.4 mm. The length of the inclined wall of the star-shaped cell, L_b , is 4.3 mm. The wall angle of the cell, θ , is 30° . Note-worthy, the structure is designed with additional upper and lower plates, which can better restore the actual application of working conditions and better filling fluid.

2.2. Mechanical properties of 6061-T6 and SSH under quasi-static loading

The schematic diagram of the tensile experiments (Exp) and the results for the matrix material, 6061-T6 aluminum alloy, used in the 3D printing of SSH structures are shown in Fig. 2. The tensile specimens were designed and fabricated according to ASTM E8M standards, with the consistent thickness of 0.5 mm from the SSH structure. The total length, parallel length, width of the tensile specimens are 200 mm, 100 mm and 12.5 mm, respectively. All test specimens were stretched at the loading velocity of 1 mm/min, and the extensometer is used to accurately measure strain. The main purpose of the uniaxial tensile test on 6061-T6, which was to obtain data for FE simulation and parametric analysis for SSH structures.

The SSH structure was tested to quasi-static compression testing using universal testing machine, with the compression velocity set at 2 mm/min. We established the FE model of SSH under the same working conditions as the quasi-static compression experiments, using the FE method similarly to other studies [10,56]. For the 6061-T6 aluminum alloy, its density $\rho_a = 2700 \text{ kg/m}^3$, Young's modulus $E_0 = 69 \text{ GPa}$, Yield strength $\sigma_y = 267 \text{ MPa}$, and Poisson's ratio $\nu_0 = 0.33$. Meanwhile, the simulation results with the mesh sizes of 0.08 mm, 0.1 mm, and 0.12 mm were compared to verify the mesh convergence of the model. As shown in Fig. 3 (a), the simulated stress-strain response of the SSH structure using a mesh size of 0.1 mm agrees well with the experimental results. In addition, the simulated deformation behaviors of the SSH at strains of $\epsilon = 0.3$ and $\epsilon = 0.6$ are consistent with the experimental results, as shown in Fig. 3 (b). Numerical results also revealed the significant NPR effect of SSH under quasi-static loading, with the peak Poisson's ratio of -0.44.

2.3. Material properties of STF

STF with particle mass fraction of 68 % was prepared by mixing SiO_2 nanoparticles with proper amount of PEG-200, with the density $\rho_s = 1640 \text{ kg/m}^3$. The specific fabrication process of STF was outlined in previously published study [60,61]. In addition, PEG-filled SSH (SSH-PEG) was selected as a constant viscosity fluid to further validate the unique coupling mechanism of SSH-STF, with the density of 1130 kg/m^3 and the viscosity of $0.052 \text{ Pa}\cdot\text{s}$ [62]. Nanoparticle characterization was conducted using Zeiss Ultra 55 (Zeiss, Germany)

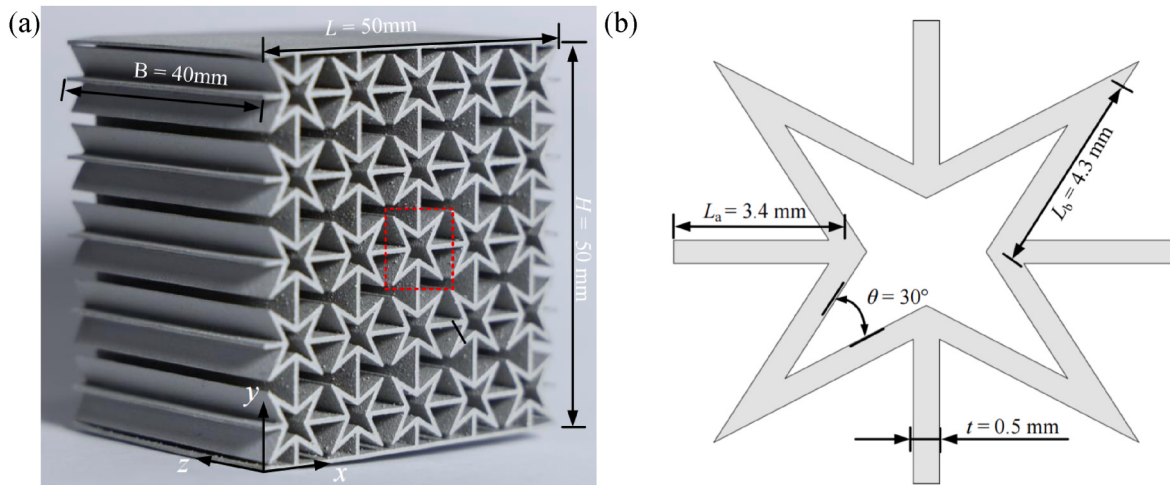


Fig. 1. Schematic diagram of (a) SSH specimen and (b) typic unit cell of SSH.

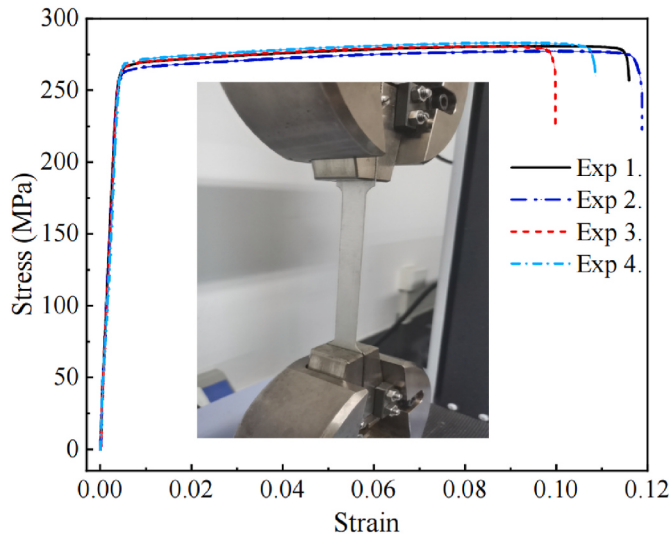


Fig. 2. Stress-strain curve of 6061-T6 matrix tensile specimens.

field-emission scanning electron microscope. The rheological analysis of STF was performed with Kinexus Pro rotary rheometer (Malvern, UK) at 25 °C, using a 40 mm diameter cone with the 1° angle and the gap of 0.03 mm. The results are shown in Fig. 4, SiO₂ nanoparticles are nearly

monodisperse, with the average diameter of 200 nm. Similar to other non-Newtonian fluids, STF shows shear thinning at lower shear rates, whereas rapid shear thickening behavior occurs when the shear strain rate exceeds the critical value of 27 s⁻¹.

In addition, the relationship between the shear viscosity of $\eta(\dot{\gamma})$ and shear strain rate of $\dot{\gamma}$ for the 68 % STF was further fitted using the power-law model, expressed as $\eta(\dot{\gamma}) = m\dot{\gamma}^{n-1}$, where m and n are material constants. Through testing data fitting in the shear-thinning phase, the constants were determined as $m = 16$ and $n = 0.47$ at the shear thinning stage. Generally, the viscosity of STF with continuous shear thickening behavior will drop again when the shear rate is very high, and the viscosity of STF with discontinuous shear thickening behavior would increase with increasing shear rate, followed by yield and even crack initiation and propagation as a solid at very high shear rate. In this paper, STF with discontinuous shear thickening behavior is employed. As it is difficult to obtain the dynamic behavior of the STF in the shear thickening regime, we assume that the viscosity of the STF increases with increasing shear rate based on our previous study [62]. With this method, the simulation results agree well with the experimental results.

2.4. Fabrication of SSH-STF and modified SHPB testing methods

The balloon with a thickness of 0.02 mm is used to effectively seal STF within SSH. It has negligible influence on the mechanical properties of the SSH-STF and can therefore be treated as a free boundary condition, as the elastic modulus of the balloon is only 0.5 MPa [61]. As

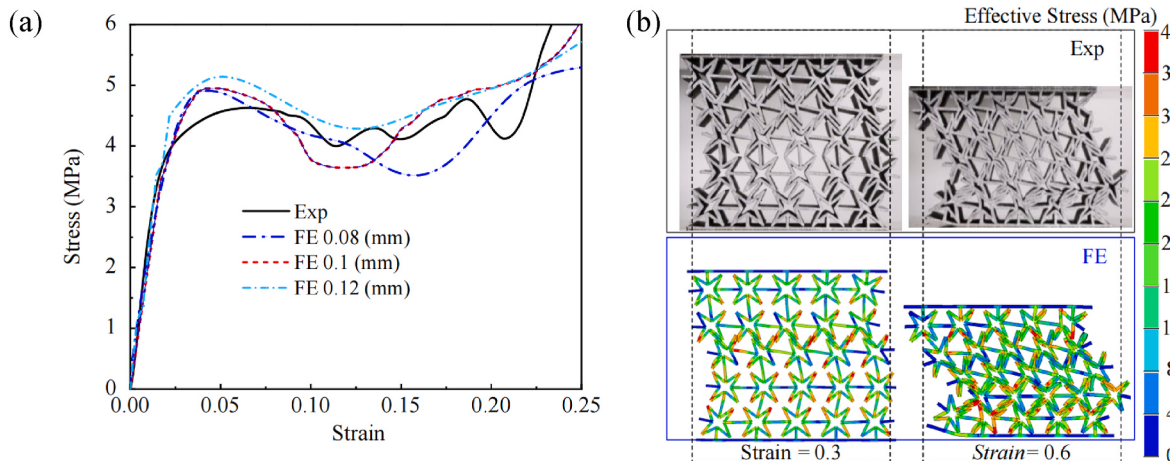


Fig. 3. Comparisons of (a) stress-strain curves with different mesh sizes and (b) deformation patterns between simulations and experiments of the SSH.

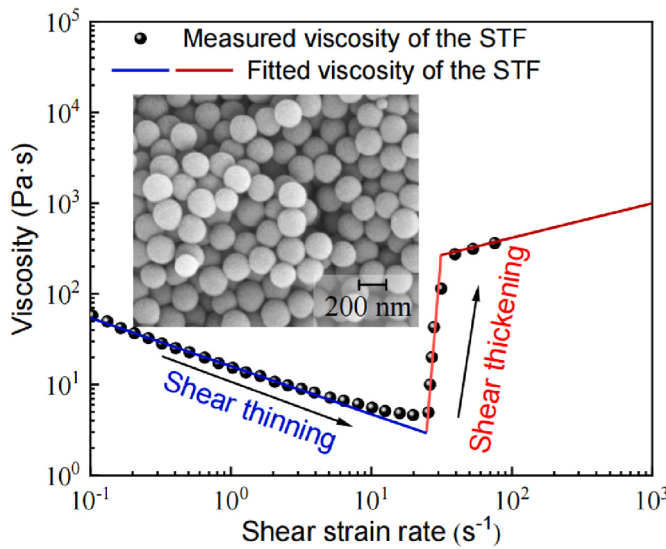


Fig. 4. Steady-state shear viscosities of the STF and the characterization of SiO_2 nanoparticles.

shown in Fig. 5(a) and (b), a 5-inch balloon is appropriately cut and stretched to accommodate exactly the SSH structure. The fluid is then injected slowly through a syringe until the structure is fully filled, as shown in Fig. 5(c).

Fig. 6 shows the experimental setup of the modified SHPB testing for SSH-STF and the corresponding schematic diagram. The prepared SSH-STF, shown in Fig. 6(a), is secured to a transmitted bar measuring $\Phi 80 \times 4000$ mm with transparent tape for the modified SHPB test setup. The transmitted bar is made of 7075 aluminum alloy with a yield stress of 510 MPa, which can be regarded as a rigid support compared to 6061-T6 and is supported by Teflon holders. A hollow cylindrical iron mass block, weighing 1 kg with dimensions of $\Phi 80 \times 100$ mm, was used to impact the SSH. The mass block was launched and velocity-controlled using an acrylic round tube of the same diameter, which connected to the gas gun. In addition, high-velocity photography was employed to capture the velocity and displacement of the mass block during testing, while strain gauges attached to the strain gages on the transmitted bar were used to calculate the force-displacement curve during dynamic loading.

In the modified SHPB test, high-pressure gas is used to accelerate the mass block, which impacts the SSH-STF specimen at a pre-determined velocity. The impact generates an elastic compressive wave, which propagates into the transmitted bar with a strain distribution denoted as $\varepsilon(t)$. Based on the one-dimensional elastic wave propagation equation, the compression process, which is considered to be in equilibrium, will be verified in subsequent results, and then the engineering stress σ can

be calculated as

$$\sigma = E \frac{A_0}{A_S} \varepsilon(t). \quad (1)$$

Where A_0 and A_S are cross-section areas of the specimen and the transmitted bar, respectively, E is the modulus of elasticity of the transmitted bar.

The compression displacement of the mass block (δ_1) is captured using high-velocity photography, while the displacement of the transmitted bar face is relatively small. Based on the relationship between the stress wave and impact velocity, $\varepsilon(t) = \rho_0 c_0 v_{st}$, and $c_0 = \sqrt{E/\rho_0}$, where ρ_0 and c_0 are density and longitudinal wave velocity in the incident bar, v_{st} is the velocity of the transmitted bar face. Then we can obtain the displacement of the transmitted bar face

$$\delta_0 = 2 / c_0 \int_0^t \varepsilon(t). \quad (2)$$

The relative displacement of the SSH-STF impact surface can be expressed as $\delta = \delta_1 - \delta_0$.

2.5. Numerical model

The FE model by ANSYS LS-DYNA was created to represent the SSH-STF specimen, with a rigid bottom plate and a cylindrical rigid upper plate, as shown in Fig. 7. The rigid cylinder retained freedom only in the compression direction (Y-direction). As the impedance of the transmitted bar is about 62 times that of SSH (see Appendix A), it was simplified to a rigid plate with all degrees of freedom fixed. Notably, the balloon was neglected when establishing the numerical model, as gravity was not considered in the model. Whereas Lagrangian hexahedral solid elements were used for both the upper and lower rigid bodies, while the SSH structure was modeled with Belytschko-Tsay shell elements. The friction coefficient of 0.2 was applied for the solid mesh contact settings, and the *CONTACT_AUTOMATIC_SURFACE_TO_SURFACE method was used for defining the contact algorithm. ALE mesh can effectively simulate the fluid characteristics of STF, water and air, with the mesh size of 0.8 times that of the Lagrangian elements in the SSH to avoid fluid penetration [63,64]. SSH-STF is simulated using the coupled Lagrange-Euler method. Coupling between the fluid and structure is achieved using the *CONSTRAINED_LAGRANGE_IN SOLID method. Each Lagrangian element is coupled at three points to ALE mesh to ensure accurate interaction. In addition, to ensure the continuity of displacement, velocity, and acceleration at the fluid-solid interface, shared nodes are used at the boundary between the STF and air.

The basic mechanical properties of 6061-T6 were obtained from tensile experiments and are modeled using the *MAT_024 model in LS-DYNA, which simulates elastic-perfectly plastic behavior. The strain-

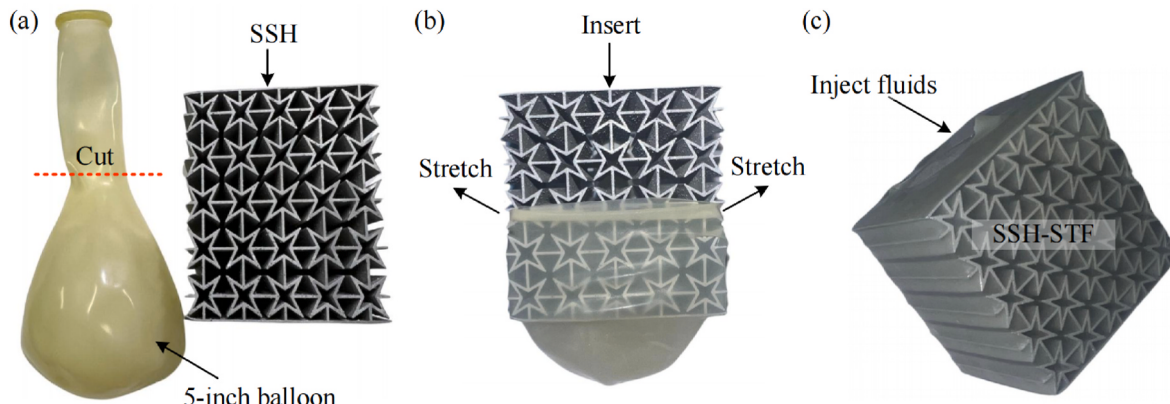


Fig. 5. Schematic diagram of the preparation process of SSH-STF.

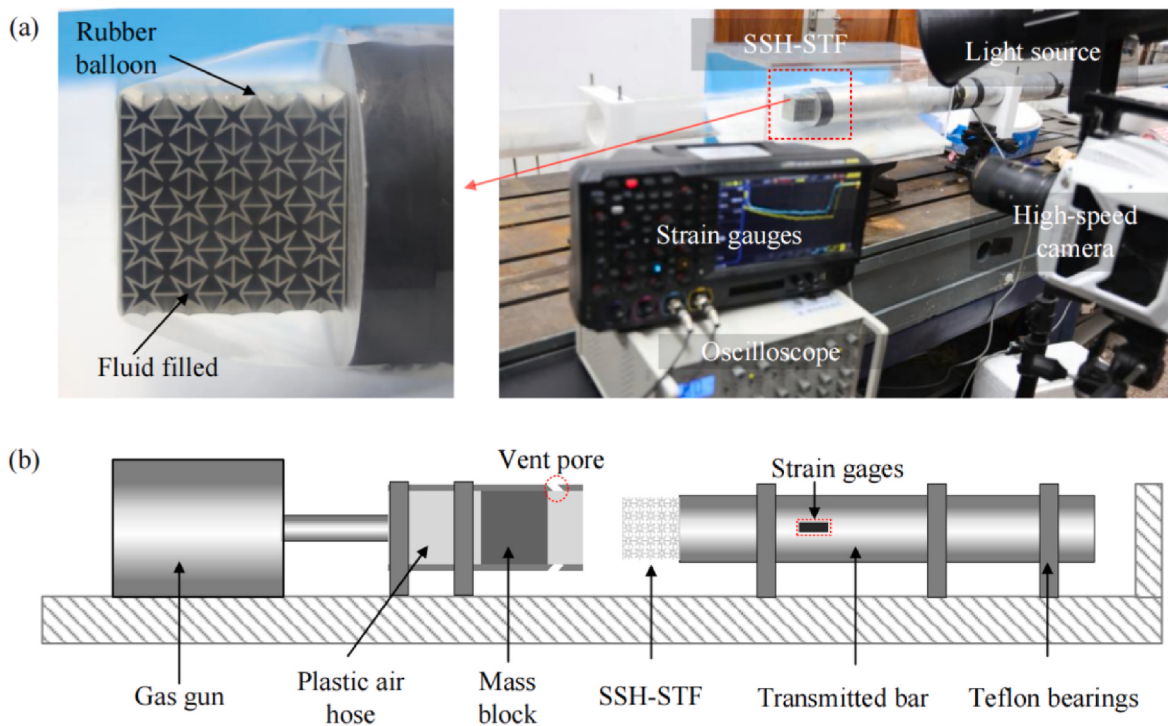


Fig. 6. Modified SHPB test for SSH-STF of (a) testing apparatuses of and (b) Schematic diagram.

rate sensitivity coefficients, C and P, were determined based on previous research [65]. The rheological properties of STF were modeled using the *MAT_ALE_VISCOUS material model, with detailed parameters for STF, water, and air, as well as their equations of state (EOS), as presented in our prior work [45]. Notably, the FE model of the SSH-STF was validated by the results of the SHPB experiment, as shown in Figs. 8–10.

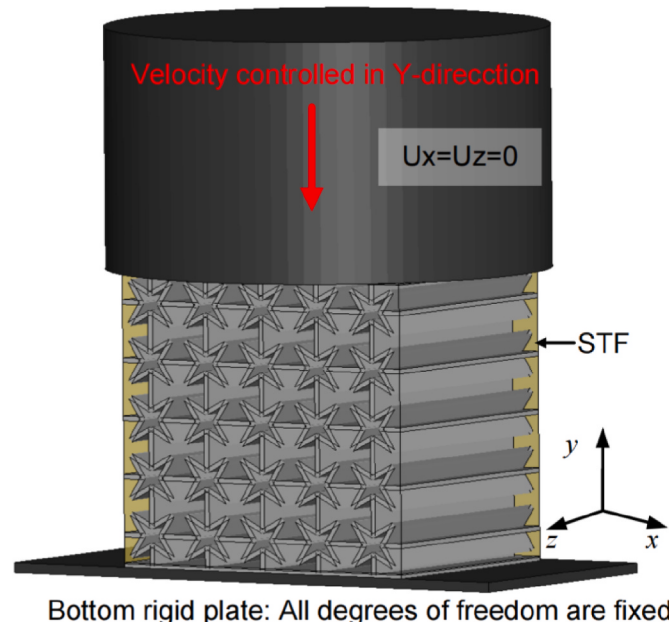
3. Results and discussions

3.1. SHPB test analysis for SSH and SSH-STF

3.1.1. Deformation model of SSH and SSH-STF

Fig. 8 shows the modified SHPB experimental deformation processes for the SSH and SSH-STF at impact velocity of 20 m/s, with strains of 0.05, 0.1, and 0.2, where strain is defined as δ/H . The deformation modes of SSH and SSH-STF are significantly different, with SSH-STF demonstrating uniform and stable compression, while SSH shows noticeable cell sliding. For further details, the deformation process of SSH and SSH-STF can be found in supplementary material of Videos 1 and 2.

With the increasing strain from 0.05 to 0.2, SSH consistently exhibits an uneven deformation mode during compression, while the in-plane sliding behavior, occurring layer by layer, is primarily governed by the third-layer unit, as shown in Fig. 8(a). In contrast, SSH-STF consistently maintains uniform compression deformation mode. As the cells undergo contraction, the STF is squeezing out, resulting in shear thickening effect. This process leads to the aggregation of nanoparticles in STF under dynamic compression, forming particle clusters [66]. Consequently, there is a change in the optical properties of STF, resulting in the whitening effect, as shown in Fig. 8(b). Furthermore, by using the bottom plates of the SSH structure as representative contact surfaces for evaluating the coupling with STF, we do not observe the fluid leakage or grid penetration, implying that the fluid and the structure remain effectively coupled (see Appendix B). Comparison of the compression velocity attenuation shows that SSH has velocities of 19.3 m/s, 17.6 m/s, and 12.6 m/s at strains of 0.05, 0.1, and 0.2, respectively, while the corresponding velocities for SSH-STF are 18.6 m/s, 11.2 m/s,



Bottom rigid plate: All degrees of freedom are fixed

Fig. 7. Numerical model of SSH-STF.

and 0.32 m/s.

Meanwhile, SSH filled with water (SSH-Wt) was represented as Newtonian fluid, in contrast to the behavior of STF, as shown in Fig. 9, with the detailed deformation process available in Supplementary material of Video 3. The deformation process of SSH-Wt is similar to that of SSH, indicating no significant improvement in energy dissipation performance compared to SSH. The attenuation process of compression velocities of 17.4 m/s, 15.4 m/s, and 11.4 m/s at strains of 0.05, 0.1, and 0.2, respectively, shows only slight differences compared to SSH. The NPR effects of SSH and SSH-Wt also show similar results, with NPR peaks of -0.42 and -0.44, respectively, while the NPR peak of SSH-STF

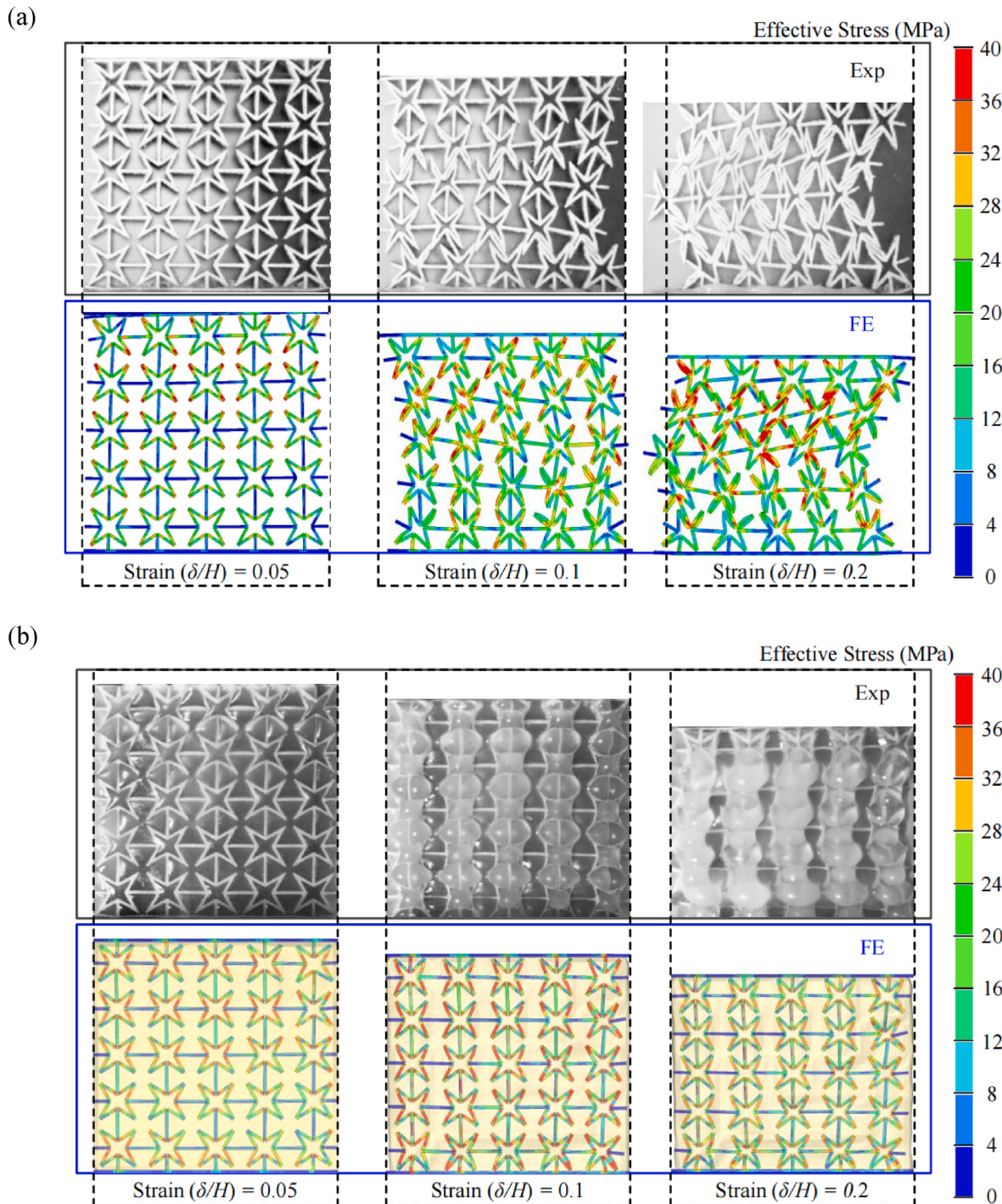


Fig. 8. Deformation pattern of experiment and FE for the SSH and SSH-STF of SHPB testing results, (a) SSH and (b) SSH-STF.

is slightly lower at -0.36 .

3.1.2. Analysis of mechanical response results for SSH and SSH-STF

The histories of compression displacement and reaction force of SSH, SSH-Wt, and SSH-STF from the SHPB tests are shown in Fig. 10. In contrast to SSH and SSH-Wt, SSH-STF shows significantly energy absorption characteristics with smaller compression displacement and higher peak force. Notably, the FE model accuracy is verified, as the FE results exhibit trends consistent with the SHPB experimental data, with errors less than 5 %. Figs. 8 and 9 further show the consistency between the experimental and FE deformation processes. The stress equilibrium is also validated by the consistency between the reaction force at the

bottom surface and deformation process from the FE model and the experimental results.

Fig. 10(a)–(c) show the comparison of the time-displacement and time-reaction force curves for SSH, SSH-Wt, and SSH-STF, respectively. The compression displacement of SSH increases almost linearly over time, while the reaction force shows significant fluctuations due to structural sliding and instability (Fig. 8(a)). Notably, filling the SSH with water enhances its initial stiffness, as demonstrated by the higher initial peak force of SSH-Wt in Fig. 10(b) compared to SSH in Fig. 10(a). However, as compression continues, the reaction force rapidly declines and eventually levels off with SSH. This indicates that water contributes little to energy absorption during sustained compression, resulting in the

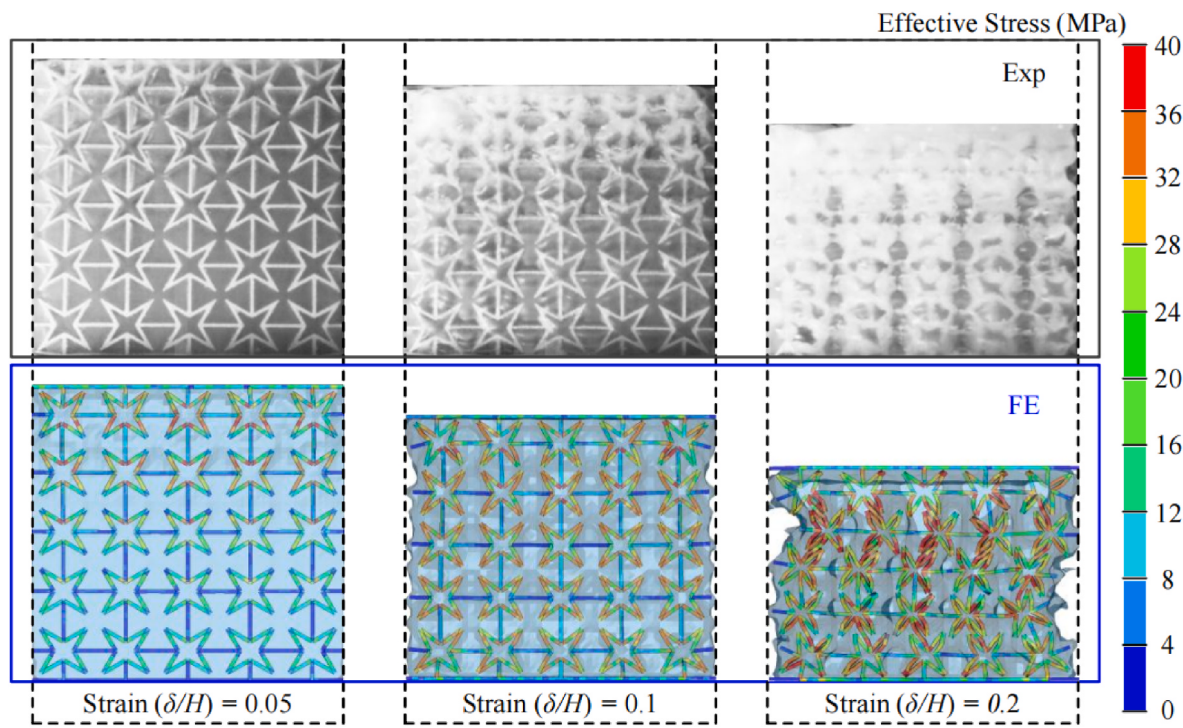


Fig. 9. Deformation pattern of experiment and FE for the SSH-Wt of SHPB testing results.

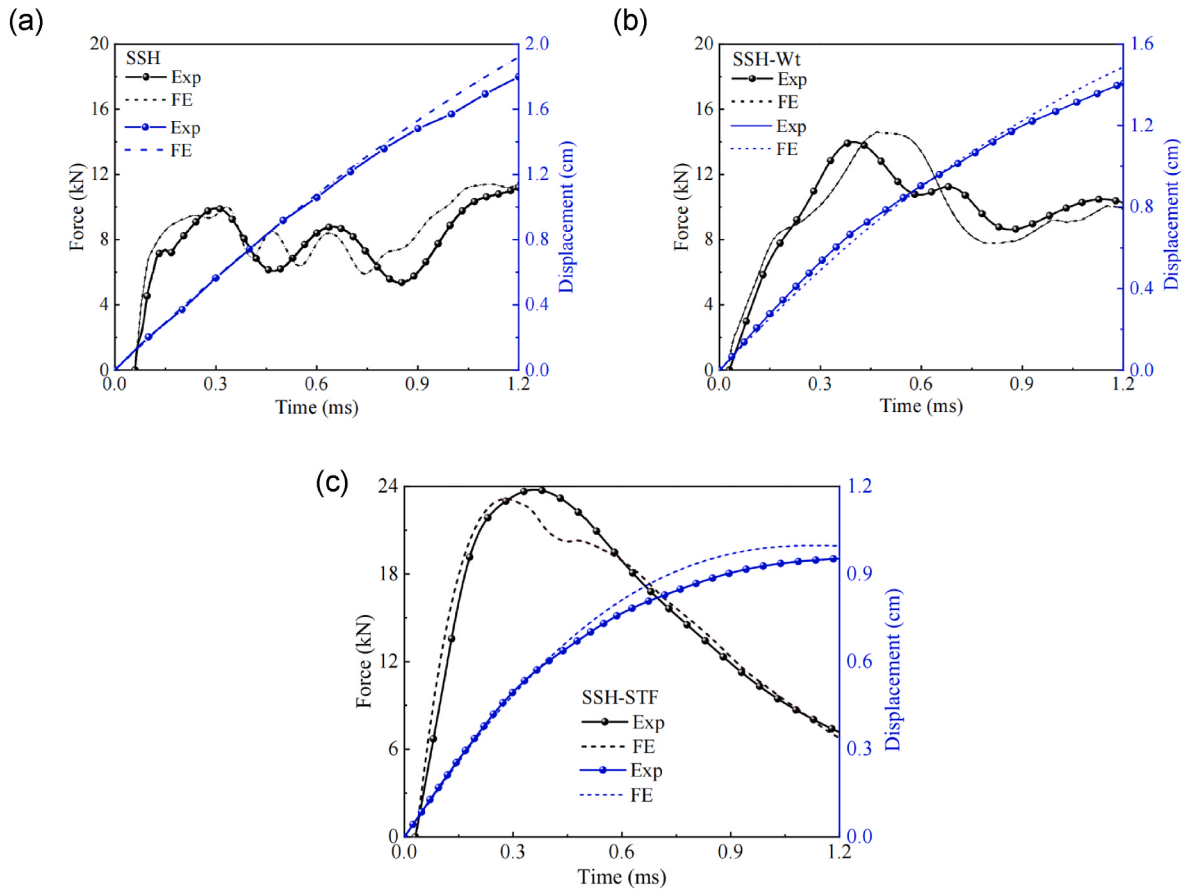


Fig. 10. Relationship of time-displacement and time-reaction force curves for (a) SSH, (b) SSH-Wt and (c) SSH-STF.

time-displacement curve similar to SSH. In contrast, SSH-STF demonstrates significant structural stiffness and energy absorption efficiency, with the force rapidly rising to a peak of 24 kN, which is 2.4 times that of SSH, followed by a rapid decline. The results can be explained by the deformation pattern and stress distribution shown in the FE results in Fig. 8(b). The stress distribution in SSH-STF reaches its peak at 0.1 strain but drops significantly by 0.2 strain. While the stress distribution in SSH continues to increase steadily throughout the compression process. This indicates that the SSH-STF dissipates energy through the overall structural response during compression from 0.05 to 0.1 strain, whereas at 0.2 strain, the structure almost completely absorbs and dissipates energy.

3.2. Dynamic mechanical response of SSH filled with different fluids

To comprehensively explore the energy absorption enhancement mechanisms resulting from the coupling of the NPR-effect SSH structure with STF, conducting systematic numerical analysis of dynamic constant-velocity V_c compression is essential. The selection of velocities for the dynamic compression numerical analysis was based on the critical velocities of the honeycomb structure, which are determined by its deformation mode [67]. The first critical velocity, at which the transition from global to localized deformation occurs, is based on the 'wave trapping' theory proposed by Hönig [68] and can be defined as

$$v_{cr1} = \int_0^{\varepsilon_{cr}} \sqrt{\sigma'(\varepsilon) \cdot \frac{1}{\rho_a} d\varepsilon}, \quad (3)$$

where ε_{cr} is the critical strain at the tangent modulus of the stress-strain curve becomes null, and the $\sigma'(\varepsilon) = \sigma_y/\varepsilon_{cr}$ is the elastic modulus of the

cellular material.

As the impact velocity increases, the honeycomb structures transition from localized deformation to progressive layer-by-layer collapse, the phenomenon defined by the second critical velocity. The second critical velocity is derived using the "steady wave" theory [69] and be expressed as

$$v_{cr2} = \sqrt{2\sigma_y \varepsilon_d \cdot \frac{1}{\rho_a}}, \quad (4)$$

where ε_d is densification strain [70]. From Eqs. (3) and (4), the first and second critical velocities (V_c) are determined to be 5 m/s and 20 m/s for the SSH. The velocity of 50 m/s chosen as a high-velocity impact to clearly contrast localized deformation with layer-by-layer collapse. Moreover, the loading time (T) can be obtained by dividing the compressive displacement (δ_c) by the constant velocity (V_c), $T = \delta_c/V_c$.

Therefore, the parameter Specific Energy Absorption (SEA) and the Mean Crushing Force (MCF) were used for analysis to quantitatively compare SSH and SSH-STF with different masses [71]. The SEA is the integral of the compressive displacement and reaction force (F), divided by the mass of the structure, m_0 , as

$$SEA = \frac{\int_0^{\delta_c} F(\delta) d\delta}{m_0}. \quad (5)$$

MCF can be expressed as

$$MCF = \frac{\int_0^{\delta_d} F(\delta) d\delta}{\delta_d}, \quad (6)$$

where δ_d is the densification phase displacement.

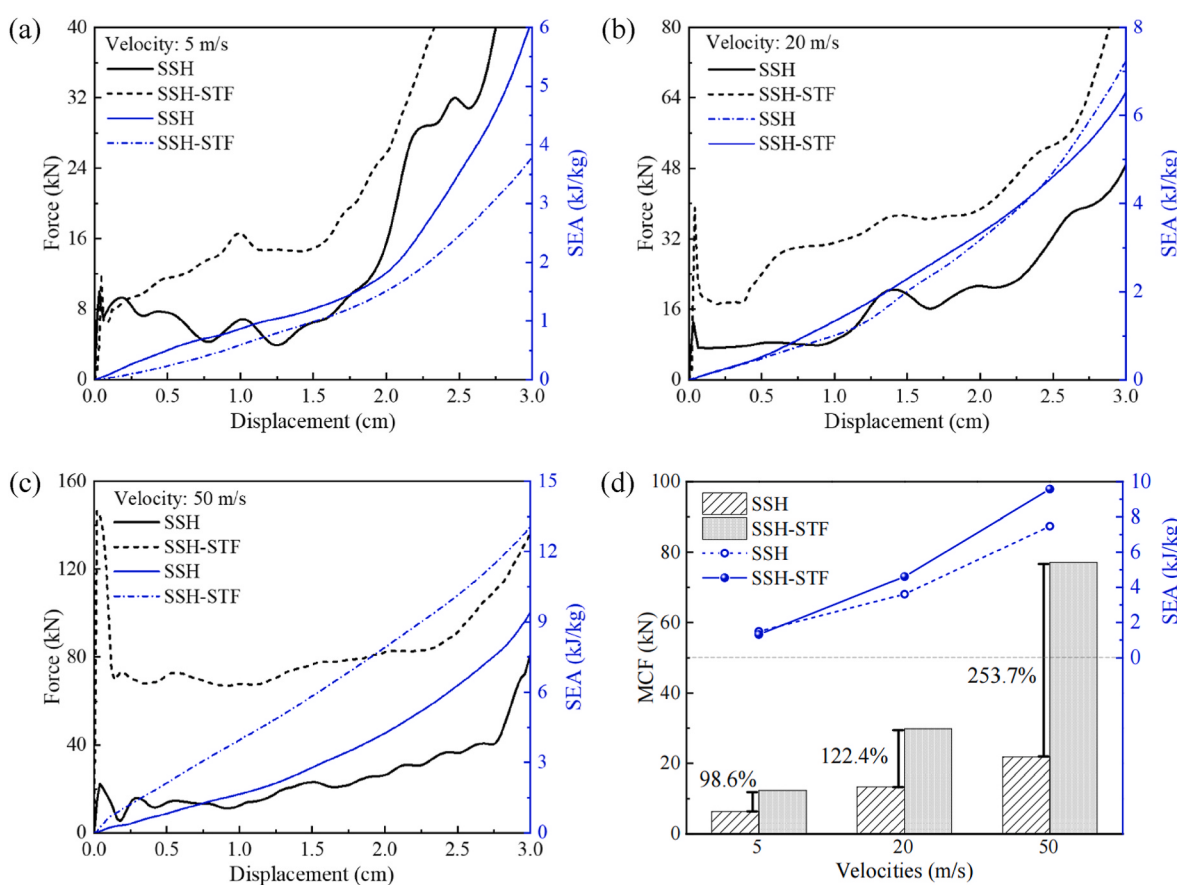


Fig. 11. Displacement-force and displacement-SEA curves under dynamic compression velocities for SSH and SSH-STF at (a) 5 m/s, (b) 20 m/s and (c) 50 m/s, with comparison of velocities with MCF and SEA shown in (d).

3.2.1. Energy absorption behaviors of SSH and SSH-STF

Fig. 11 shows the upper surface reaction force, SEA, and MCF of SSH and SSH-STF under dynamic compression velocities. SSH-STF consistently exhibits the highest force and MCF, with its advantage becoming more pronounced as the compression velocity increases, except in the compression displacement range of 0.1–0.2 cm, where the force is lower than SSH (see Appendix C for the reason for the higher force in SSH than in SSH-STF). However, the SEA of SSH-STF remains lower than that of SSH at 5 m/s, as shown in **Fig. 11(a)**. As the velocity rises to the second critical velocity, the SEA of SSH-STF surpasses that of SSH, with a more pronounced contrast between the two observed at 50 m/s, as shown in **Fig. 11(b)** and (c). In addition, comparing the increasing trends of SEA during the densification phase, it can be observed that SSH-STF's SEA rises more slowly than SSH.

The influence of velocity on MCF and SEA for SSH and SSH-STF during the densification phase is more clearly compared in **Fig. 11(d)**. SSH-STF consistently outperforms SSH in terms of MCF, even with 253.7 % higher at 50 m/s. Compared to the slower increase in SEA for SSH, the SEA of SSH-STF increases linearly with the rising compression velocities.

3.2.2. Deformation characteristics with SSH and SSH-STF

The deformations mode and stress distribution of SSH and SSH-STF during the densification phase are shown in **Fig. 12**. As compression velocity increases, SSH-STF shows more uniform and regular deformation pattern, with higher level and more uniform stress distribution than SSH.

The SSH and SSH-STF show similar deformation modes at 5 m/s. However, as the velocity increases, SSH undergoes disordered densification due to irregular cell stacking, whereas SSH-STF shows more regular deformation pattern. Particularly at 50 m/s, the deformation of individual cells becomes nearly uniform and fully contracted, demonstrating enhanced structural stability and high responsiveness under high-velocity impacts.

3.2.3. Energy absorption behaviors of SSH filling Newtonians fluids

To further validate the distinct coupling mechanism of STF, we

compared SSH filled with water and PEG with STF at 50 m/s, as shown in **Fig. 13**. The results demonstrate that the peak forces of SSH-Wt and SSH-PEG increases slightly due to the inertial effect of the filled Newtonians fluids. However, the SEAs of SSH-Wt and SSH-PEG decreases largely due to the weak fluid-solid interaction. In contrast, the strong interaction between SSH and STF after occurrence of shear thickening of STF results in a significant platform force and SEA, approximately 2.2 times and 1.4 times higher than that of SSH-PEG and SSH-Wt, respectively.

3.3. Coupling mechanism of SSH-STF

Filling STF into SSH significantly enhances its energy absorption and deformation stability. To elucidate the underlying mechanism, this section analyzes the coupling behavior between SSH and SSH-STF.

3.3.1. Shear thickening effect of STF under dynamic loading

Fig. 14 shows the distribution of shear strain rate in SSH-STF at the strain of 0.1 and compression velocities of 5 m/s, 20 m/s, and 50 m/s. As the velocity increases, the shear strain rate shows significant sensitivity.

At the compression velocity of 5 m/s, the overall shear strain rate distribution of STF is slight, with the peak shear strain rate being only about 20 s^{-1} , which is lower than the shear thickness threshold of 27 s^{-1} . Thus, the STF filling does not have a significant effect on the SSH structure. This demonstrates that the SEA curve of SSH-STF is lower than SSH at 5 m/s (**Fig. 11(a)**).

As the compression velocity increases to 20 m/s, the shear strain rate increases significantly, with the primary concentration occurring in the unit cells of the SSH structure. The highest shear strain rates are observed at the center of the unit cells and the outer edges of the cell walls, with the overall strain rate reaching 200 s^{-1} .

The shear strain rate distribution exhibits extremely high levels, with a distinct and regular pattern at 50 m/s. All the unit cells of SSH display similar deformation models. High shear strain rate regions are located both within the unit cells and around the wall corners, where the shear strain rate in STF reaches about 1600 s^{-1} . In contrast, shear strain rate in STF near the horizontal connecting walls between the unit cells is

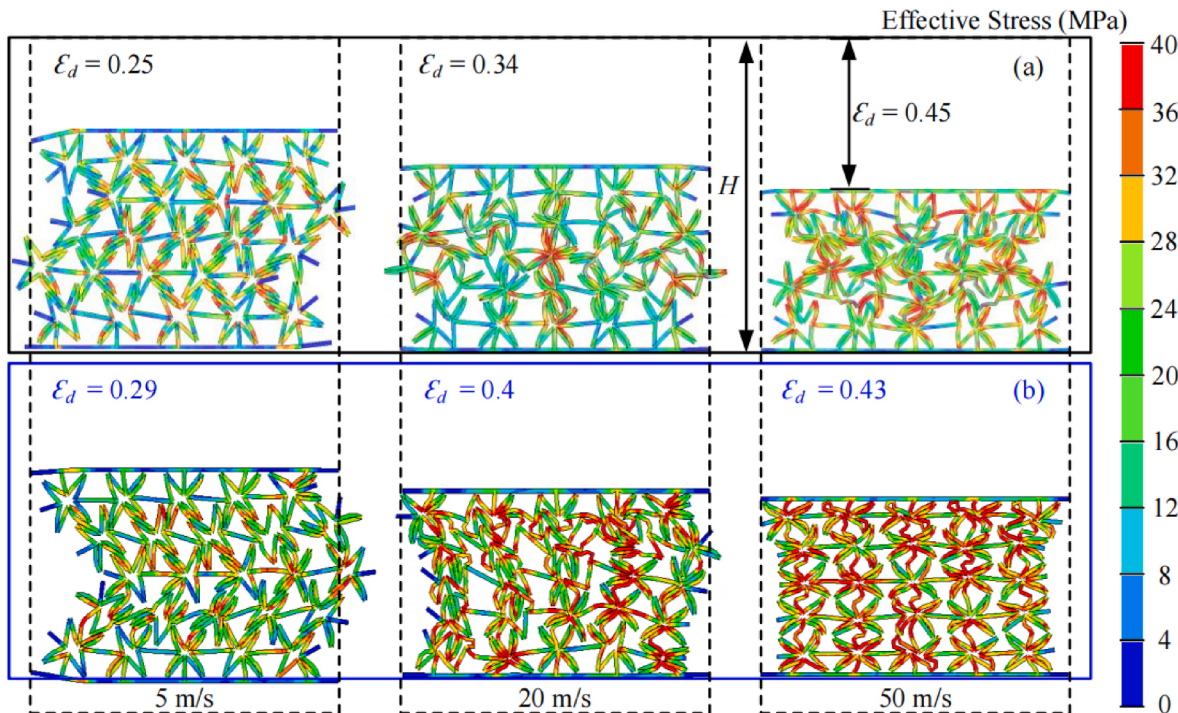


Fig. 12. Deformation modes of (a) SSH and (b) SSH-STF during the densification phase.

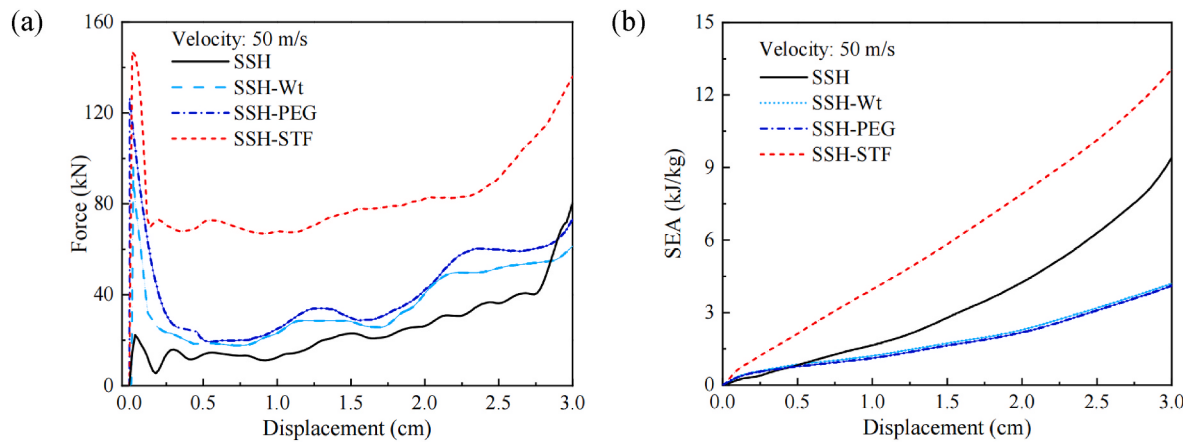


Fig. 13. Energy absorption performance of SSH filled with STF and Newtonian Fluids.

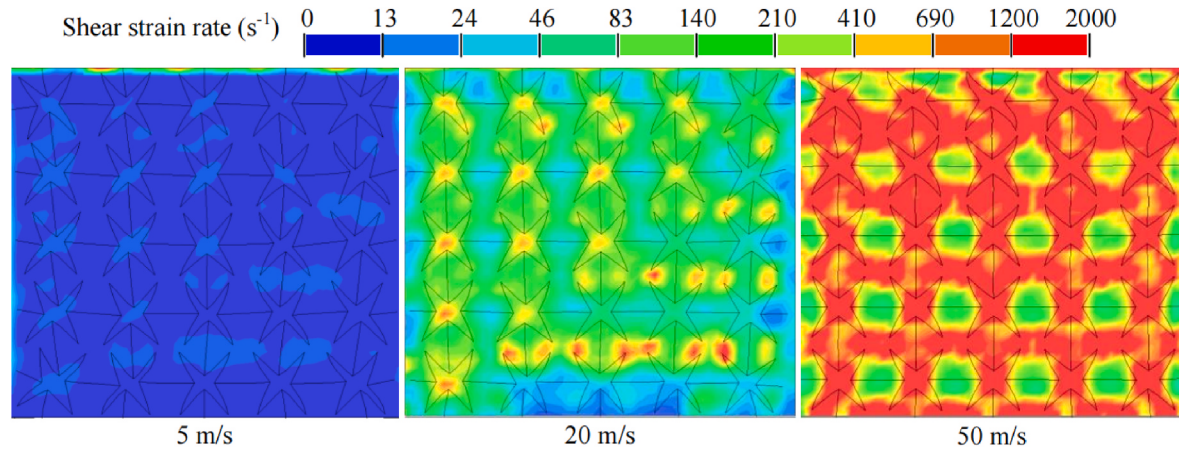


Fig. 14. Shear strain rate distribution of STF filled in the SSH structure at strain of 0.1 and compression velocity of 50 m/s.

relatively lower, at about 200 s^{-1} . With the significant shear thickness effect of STF in the SSH structure, the SSH-STF demonstrates superior energy absorption efficiency compared to SSH (Fig. 11(c)).

Meanwhile, we obtained the strain rate distributions of SSH-STF, as shown in Fig. 15. With the increase of impact velocity, the strain rate of the SSH structure increases from approximately 5 s^{-1} at 5 m/s to about 100 s^{-1} at 50 m/s. Notably, SSH filled with STF exhibits more uniform strain rate distribution at 50 m/s compared to 5 m/s and 20 m/s. This indicates that the shear thickening effect of STF significantly enhances the overall stability and mechanical response of SSH under higher impact velocity.

The strain rate distribution of SSH filled with Newtonian fluids under high-velocity impact further manifests the unique role of STF. As shown in Fig. 16, compared to SSH-STF the non-uniform distribution of strain rate for SSH, SSH-Wt, and SSH-PEG at 50 m/s at the strain of 0.1 indicates the layer-by-layer collapse dominated deformation pattern, showing that the Newtonian fluids have slight effects on the deformation pattern of SSH under high-velocity impact.

3.3.2. Energy absorption enhanced mechanism of SSH coupling with STF

The energy enhancing coupling mechanism between STF and SSH can be further clarified by analyzing the deformation process of the

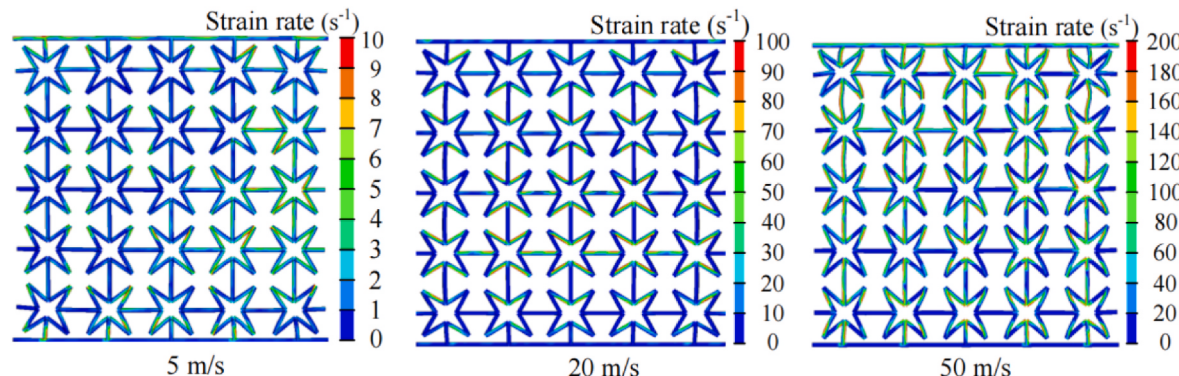


Fig. 15. Strain rate distribution of SSH in SSH-STF structure at strain of 0.1 and impact velocity of (a) 5 m/s, (b) 20 m/s and (c) 50 m/s.

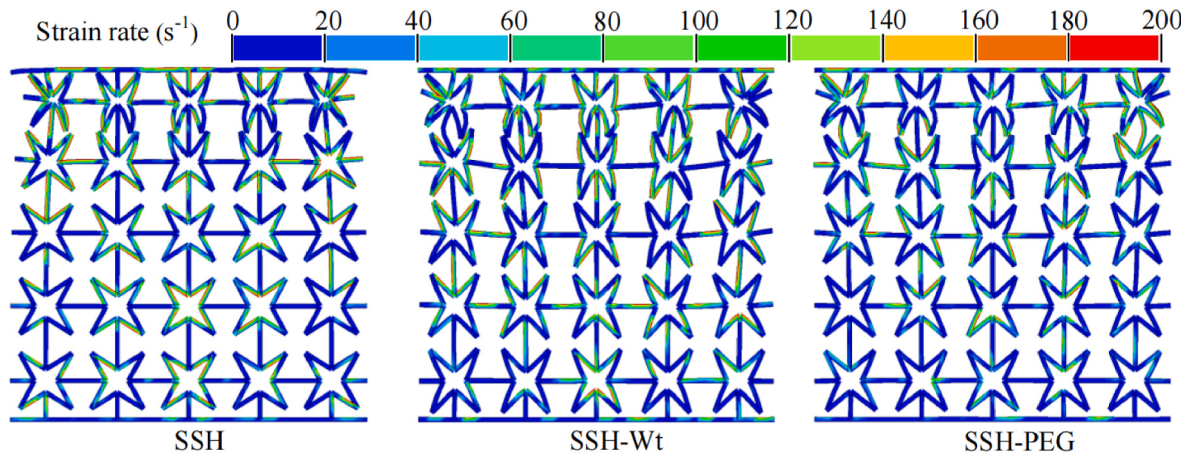


Fig. 16. Strain rate distribution of SSH filled with different Newtonian fluid.

typical unit cell at 50 m/s, as shown in Fig. 17. With strains from 0.05 to 0.3, the unit cell of SSH-STF shows higher stress levels and more stable compression deformation process compared to SSH.

Fig. 17(a) shows that the unit cell of SSH undergoes in-plane contraction and rotational deformation process. The stress distribution concentration mainly occurs at the locations where several plastic hinges form, similarly to other research [59,72]. By measuring the rotational angle of the unit cell's side walls, as depicted by the black dotted lines, the relative rotation of 45° is observed during the strains from 0.05 to 0.3. Meanwhile, the horizontal ribs experience a relative rotation of 12°, which contributes to a certain level of contraction behavior in the horizontal direction of the unit cell.

With the coupling of STF, rotational deformation resistance is demonstrated in SSH-STF, as shown in Fig. 17(b). The relative rotation of the unit cell's side walls is 8°, while the horizontal ribs experience almost disappears. This indicates that the shear thickening effect of STF significantly constrains in-plane rotational behavior in SSH-STF and the high stress distribution on the cell walls supports this observation.

Moreover, the in-plane contraction of the unit cell interacts with the compression of the STF under the constraint of rotational restraint, leading to a greater involvement of the unit cell in in-plane contraction, increasing the stress levels on the cell walls. As shown in Fig. 17(b), at the strain of 0.3, the unit cell of SSH-STF almost fully contracts, compressing STF and generating higher stress levels. This compression

results in significant stress distribution along the inner walls of the unit cell. In contrast, Fig. 17(a) shows that at the same strain, the in-plane rotation of SSH hinders contraction, creating space within the unit cell that reduces energy absorption.

Based on the above analysis, we reveal the coupling mechanism between STF and SSH, as shown in Fig. 18. Under dynamic compression, the SSH without STF unit cell exhibits in-plane rotation and contraction, leading to a significant NPR effect. After filling STF, the in-plane rotation of SSH results in the shear thickening effect of STF, which generates a reactive force that resists the in-plane rotation of the SSH unit cell, resulting in more uniform and complete in-plane contraction and significantly improving structural deformation stability. In addition, the squeezing force due to the interaction between the contraction of the SSH unit cell and the shear thickening of STF not only improves the energy dissipation efficiency of STF but also expands the deformation and energy absorption regions of SSH. As a result, the overall deformation and stress distribution of the SSH-STF become more uniform, enhancing the energy absorption of the composite.

3.3.3. Improvement of the overall structural response of SSH-STF

Fig. 19 shows the deformation process and stress distribution of SSH and SSH-STF during the compression period from 0 to 32 μs at the compression velocity of 50 m/s. The SSH-STF demonstrates more uniform deformation and accelerated stress transmission compared to SSH.

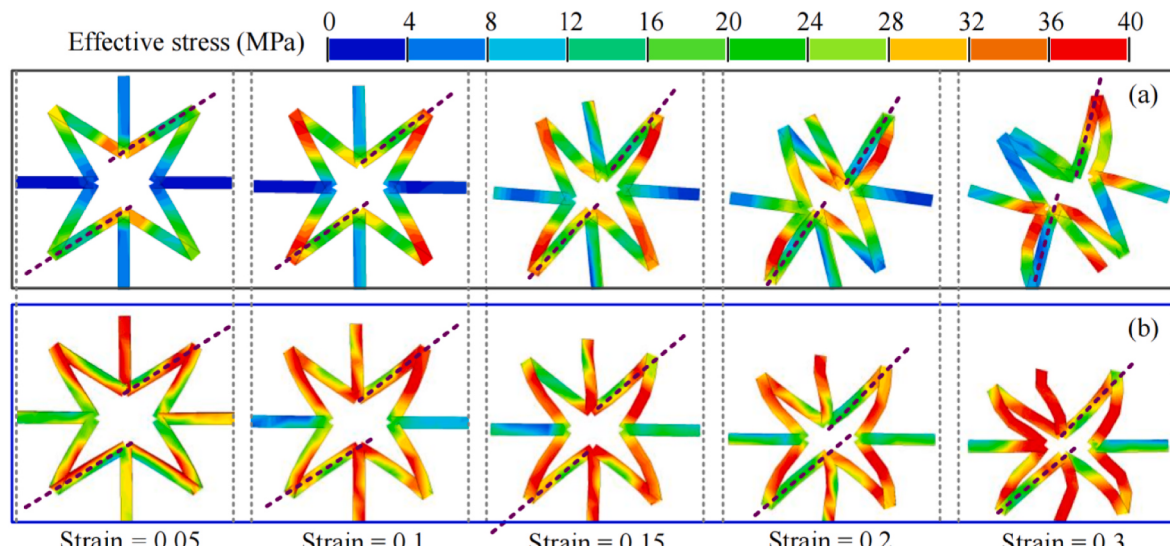


Fig. 17. Deformation process of the typical unit cell of (a) SSH and (b) SSH-STF at 50 m/s.

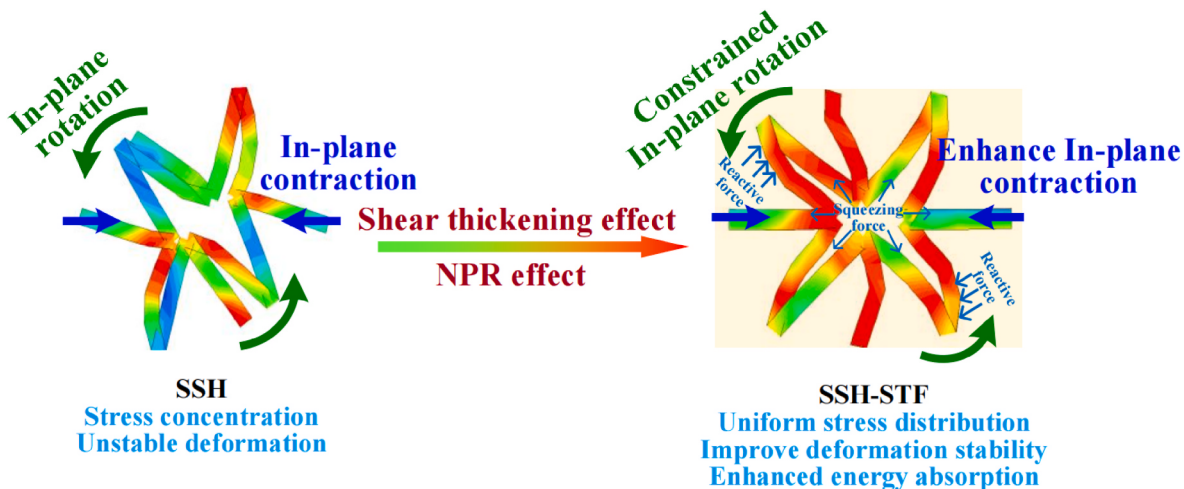


Fig. 18. Schematic illustration of the coupling mechanism of SSH-STF.

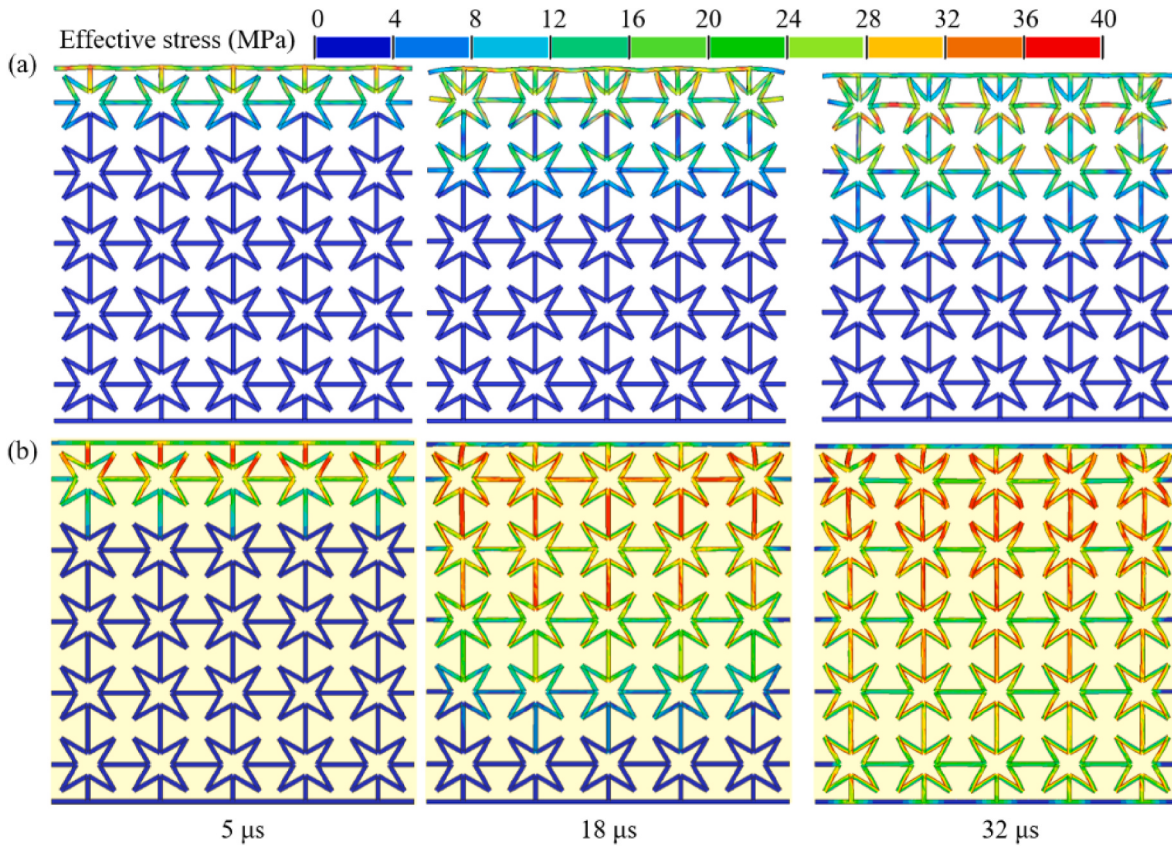


Fig. 19. Deformation process and stress distribution of (a) SSH and (b) SSH-STF under compression.

Fig. 19(a) shows that from 0 to 32 μ s, the stress transmission and deformation mode of SSH are primarily concentrated in the first layer of unit cells, displaying a clear layer-by-layer collapse. In contrast, the SSH-STF demonstrates a more uniform overall deformation, as shown in **Fig. 19(b)**, with stress transfer occurring more rapidly. At 5 μ s, the stress fully propagates through the first layer, showing higher and more evenly distributed stress levels compared to SSH. As compression continues to 18 μ s, the stress in SSH-STF has nearly reached the bottom layer. The cell walls and vertical ribs are restricted by the shear thickening STF, which interacts to generate higher stress levels. At 32 μ s, the stress was fully transferred to the bottom layer, while the unit cells undergo a slight in-plane contraction, with uniform stress concentration along the inner

walls of the cells due to the overall compression to the STF.

It demonstrates that the complex in-plane structure of SSH impedes the rapid transmission of stress, causing layer-by-layer collapse due to inertial effects under high-velocity impact. In contrast, stress is transmitted more quickly in STF [60,73], and its coupling with the SSH structure enhances overall stress distribution by facilitating rapid stress transfer within the SSH-STF. Moreover, the local shear thickening behavior of the STF limits layer-by-layer collapse, which significantly improves the local deformation stability of the SSH-STF and promotes stress equilibrium under high-velocity impact, resulting in higher critical impact velocity.

4. Conclusions

In this paper, the coupling mechanisms between STF and SSH under impact is studied. The main conclusions are as follows.

1. A new design approach for STF-filled SSH auxetic honeycomb structures is proposed, significantly enhancing energy absorption and structural stability under dynamic impacts. After filling STF, the MCF of SSH increases by 253 %, and the SEA improves by 54 %.
2. The coupling mechanism between the shear thickening effect of STF and the NPR effect of SSH is revealed, showing that the NPR effect drives a higher shear strain rate in STF due to the in-plane contraction and rotation of the SSH structure. This enhances the shear thickening effect, leading to more effective energy dissipation and improved coupling between STF and SSH.
3. The shear thickening effect of STF suppresses approximately 82 % of the in-plane rotational behavior of the SSH structure, leaving only contraction deformation. This significantly enhances the stability of the SSH structure, allowing it to fully contract and absorb energy more effectively.
4. The coupling of shear thickening in STF and compressive deformation in SSH accelerates the propagation of stress waves within the SSH structure, thereby increasing the critical impact velocity and improving the structure's performance under high-velocity impacts.
5. SSH-STF exhibits a more uniform and stable overall response under higher velocity impacts, which has not been addressed in existing research.

CRediT authorship contribution statement

J.P. Ren: Conceptualization, Investigation, Data curation, Formal analysis, Writing – original draft. **Z.P. Gu:** Investigation, Data curation, Methodology. **Y.D. Sui:** Investigation. **A.G. Zhao:** Conceptualization, Methodology. **C.G. Huang:** Conceptualization, Methodology, Funding acquisition. **X.Q. Wu:** Conceptualization, Funding acquisition, Formal analysis, Visualization, Writing – review & editing.

Declaration of competing interest

The authors declare that they have no known competing financial interests or personal relationships that could have appeared to influence the work reported in this paper.

Acknowledgments

This work was supported by the National Key R&D Program of China (Grant No. 2021YFA0719200); the National Natural Science Foundation of China (Grant Nos. 12272391, 12232020 and 12402475); the Postdoctoral Fellowship Program of CPSF (Grant No. GZC20241781 and 2024M763360); and the CAS Project for Young Scientists in Basic Research (YSBR-096).

Appendix A. Supplementary data

Supplementary data to this article can be found online at <https://doi.org/10.1016/j.compositesb.2025.112415>.

Data availability

Data will be made available on request.

References

- [1] Zhang J, Lu G, You Z. Large deformation and energy absorption of additively manufactured auxetic materials and structures: a review. Compos. Pt. B-Eng. 2020;201:108340. <https://doi.org/10.1016/j.compositesb.2020.108340>.
- [2] Li X, Peng WT, Wu WW, Xiong J, Lu Y. Auxetic mechanical metamaterials: from soft to stiff. Int. J. Extreme Manuf. 2023;5:042003. <https://doi.org/10.1088/2631-7990/ace668>.
- [3] Hu QF, Lu GX, Tse KM. Compressive and tensile behaviours of 3D hybrid auxetic-honeycomb lattice structures. Int J Mech Sci 2024;263:108767. <https://doi.org/10.1016/j.ijmecsci.2023.108767>.
- [4] Zhou JH, Lun YZ, Zhao YT, Lei HS, Lei Y, Wei K, et al. Strain-independent auxetic metamaterials inspired from atomic lattice. Int J Mech Sci 2024;281:109614. <https://doi.org/10.1016/j.ijmecsci.2024.109614>.
- [5] Montazeri A, Bahmanpour E, Safarabadi M. A Poisson's ratio sign-switching mechanical metamaterial with tunable stiffness. Int J Mech Sci 2023;260:108670. <https://doi.org/10.1016/j.ijmecsci.2023.108670>.
- [6] Zhang Q, Li M, Cai JG. A novel misplaced reinforced honeycomb with in-plane bidirectional enhancement. Int J Mech Sci 2024;270:109088. <https://doi.org/10.1016/j.ijmecsci.2024.109088>.
- [7] An MR, Wang L, Liu HT, Ren FG. In-plane crushing response of a novel bidirectional re-entrant honeycomb with two plateau stress regions. Thin-Walled Struct 2022;170:108530. <https://doi.org/10.1016/j.tws.2021.108530>.
- [8] Bohari RP, Linforth S, Nguyen T, Ghazlan A, Ngo T. Novel lightweight high-energy absorbing auxetic structures guided by topology optimisation. Int J Mech Sci 2021; 211:106793. <https://doi.org/10.1016/j.ijmecsci.2021.106793>.
- [9] Zhang CB, Lu FC, Wei TH, Huang YJ, He Y, Zhu YL. A novel windmill-shaped auxetic structure with energy absorption enhancement. Int J Mech Sci 2024;280: 109635. <https://doi.org/10.1016/j.ijmecsci.2024.109635>.
- [10] Pan YC, Sang M, Zhang JS, Li ZM, Liu S, Zhang ZT, et al. An integrative warning-protection shear thickened composite sponge towards sensing performance and impact resistance with excellent flame retardant. Compos. Pt. B-Eng. 2024;279: 111466. <https://doi.org/10.1016/j.compositesb.2024.111466>.
- [11] Hu D, Wang Y, Song B, Dang L, Zhang Z. Energy-absorption characteristics of a bionic honeycomb tubular nested structure inspired by bamboo under axial crushing. Compos. Pt. B-Eng. 2019;162:21–32. <https://doi.org/10.1016/j.compositesb.2018.10.095>.
- [12] Chen C, Airoldi A, Caporale AM, Sala G, Yin X. Impact response of composite energy absorbers based on foam-filled metallic and polymeric auxetic frames. Compos Struct 2024;331:117916. <https://doi.org/10.1016/j.comstruct.2024.117916>.
- [13] Hu Q, Zhang X, Zhang J, Lu G, Tse KM. A review on energy absorption performance of auxetic composites with fillings. Thin-Walled Struct 2024;205:112348. <https://doi.org/10.1016/j.tws.2024.112348>.
- [14] Albertini F, Dirrenberger J, Sollogoub C, Maconachie T, Leary M, Molotnikov A. Experimental and computational analysis of the mechanical properties of composite auxetic lattice structures. Addit Manuf 2021;47:102351. <https://doi.org/10.1016/j.addma.2021.102351>.
- [15] Chen M, Chen Z, Xuan Y, Zhang T, Zhang M. Static and dynamic compressive behaviour of 3D printed auxetic lattice reinforced ultra-high performance concrete. Cem Concr Compos 2023;139:105046. <https://doi.org/10.1016/j.cemconcomp.2023.105046>.
- [16] Xue Y, Wang W, Han F. Enhanced compressive mechanical properties of aluminum based auxetic lattice structures filled with polymers. Compos. Pt. B-Eng. 2019;171: 183–91. <https://doi.org/10.1016/j.compositesb.2019.05.002>.
- [17] Gao Q, Liao WH. Energy absorption of thin walled tube filled with gradient auxetic structures-theory and simulation. Int J Mech Sci 2021;201:106475. <https://doi.org/10.1016/j.ijmecsci.2021.106475>.
- [18] Airoldi A, Novak N, Sgobba F, Gilardelli A, Borovinšek M. Foam-filled energy absorbers with auxetic behaviour for localized impacts. Mater. Sci. Eng. A 2020; 788:139500. <https://doi.org/10.1016/j.msea.2020.139500>.
- [19] Farrokhabadi A, Mahdi Ashrafi M, Behravesh AH, Kaveh Hedayati S. Assessment of fiber-reinforcement and foam-filling in the directional energy absorption performance of a 3D printed accordion cellular structure. Compos Struct 2022;297: 115945. <https://doi.org/10.1016/j.compstruct.2022.115945>.
- [20] Chen M, Yao X, Zhu L, Yin M, Xiong Y, Hu N. Geometric design and performance of single and dual-printed lattice-reinforced cementitious composite. Cem Concr Compos 2023;143:105266. <https://doi.org/10.1016/j.cemconcomp.2023.105266>.
- [21] Sheikhi MR, Gürgen S, Li J, Sofuoğlu MA, Hasanzadeh M, Cemal M, et al. Design of smart sandwich structures enhanced by multi-functional shear thickening fluids (M-STFs): anti-vibration and electrical conductivity. Compos Struct 2023;324: 117520. <https://doi.org/10.1016/j.compstruct.2023.117520>.
- [22] Sheikhi MR, Hasanzadeh M, Gürgen S, Li J. Enhanced anti-impact resistance of polyurethane foam composites with multi-phase shear thickening fluids containing various carbon nanofillers. Mater Today Commun 2024;38:107991. <https://doi.org/10.1016/j.mtcomm.2023.107991>.
- [23] Deng JQ, Chen LM, Liu T, Pan X, Zheng SF, Yun ZX, et al. Crushing responses and energy absorption characteristics of the dynamic stiffening porous material subjected to different strain rates. Int J Impact Eng 2025;195:105117. <https://doi.org/10.1016/j.ijimpeng.2024.105117>.
- [24] Zhang QY, Qin ZG, Yan RS, Wei SN, Zhang W, Lu SL, et al. Processing technology and ballistic-resistant mechanism of shear thickening fluid/high-performance fiber-reinforced composites: a review. Compos Struct 2021;266:113806. <https://doi.org/10.1016/j.compstruct.2021.113806>.
- [25] Zhang JS, Wang Y, Wu JP, Zhou JY, Wang WH, Liu S, et al. STF-filled biomimetic variable stiffness hierachic porous material with impact resistance, thermal insulation, and sensing. Chem. Eng. J. 2023;477:146939. <https://doi.org/10.1016/j.cej.2023.146939>.
- [26] Waqas H, Farooq U, Muhammad T, Manzoor U. Shear thinning and shear thickening aspects in magnetized 3D cross-nanofluid flow with activation energy

- and motile microorganisms. *Waves Random Complex Media* 2022;20:1303–22. <https://doi.org/10.1080/17455030.2022.2032469>.
- [27] Long S, Chen H, Yao X, Liu T. Response of shear thickening fluids to high velocity ballistic impact. *Int J Impact Eng* 2025;105248. <https://doi.org/10.1016/j.ijimpeng.2025.105248>.
- [28] Zhang J, Wang Y, Deng H, Zhou J, Liu S, Wu J, et al. A high anti-impact STF/Ecoflex composite structure with a sensing capacity for wearable design. *Compos. Pt. B-Eng.* 2022;233:109656. <https://doi.org/10.1016/j.compositesb.2022.109656>.
- [29] Wang WJ, Yang H, Zhang WM, Shang N, Ma L. Experimental study on the impact resistance of fill-enhanced mechanical metamaterials. *Int J Mech Sci* 2025;285:109799. <https://doi.org/10.1016/j.ijmecsci.2024.109799>.
- [30] Zhang SS, Wang S, Hu T, Xuan SH, Jiang H, Gong XL. Study the safeguarding performance of shear thickening gel by the mechanoluminescence method. *Compos. Pt. B-Eng.* 2020;180:107564. <https://doi.org/10.1016/j.compositesb.2019.107564>.
- [31] Zhao CY, Wang YP, Cao SS, Xuan SH, Jiang WQ, Gong XL. Conductive shear thickening gel/Kevlar wearable fabrics: a flexible body armor with mechano-electric coupling ballistic performance. *Compos Sci Technol* 2019;182:107782. <https://doi.org/10.1016/j.compscitech.2019.107782>.
- [32] Zhang K, Gao Q, Jiang JC, Chan MS, Zhai XY, Jin LC, et al. High energy dissipation and self-healing auxetic foam by integrating shear thickening gel. *Compos Sci Technol* 2024;249:110475. <https://doi.org/10.1016/j.compscitech.2024.110475>.
- [33] Chen F, Tang ZH, Zhu Y, Deng JQ, Li YQ, Fu YQ, et al. Gradient shear thickening gel/Kevlar fabric multi-layer armor with enhanced impact attenuation property. *Compos Struct* 2024;330:117829. <https://doi.org/10.1016/j.comstruct.2023.117829>.
- [34] Lin G, Li J, Li F, Chen P, Sun W. Low-velocity impact response of sandwich composite panels with shear thickening gel filled honeycomb cores. *Compos Commun* 2022;32:101136. <https://doi.org/10.1016/j.coco.2022.101136>.
- [35] Zhou ZP, Sun WF. Mechanical behavior and failure mechanism of aerogel-reinforced carbon fibre/epoxy composites under quasi-static/impact loading. *Polym Test* 2022;115:107761. <https://doi.org/10.1016/j.polymertesting.2022.107761>.
- [36] Yang H, Ma L. Multi-stable mechanical metamaterials with shape-reconfiguration and zero Poisson's ratio. *Mater Des* 2018;152:181–90. <https://doi.org/10.1016/j.matdes.2018.04.064>.
- [37] Wang DP, Zhao CY, Yang JJ, Lai SY, Wang XY, Gong XL. Enhanced mechanical-magnetic coupling and bioinspired structural design of magnetorheological elastomers. *Adv Funct Mater* 2024;2419111. <https://doi.org/10.1002/adfm.202419111>.
- [38] Li ZM, Wang S, Wang WH, Wu JP, Zhang ZT, Li DY, et al. Nacre-inspired MMT-MXene integrated shear-stiffening gel composites for personal safeguard and multi-functional electronics. *Compos. Pt. B-Eng.* 2024;280:111526. <https://doi.org/10.1016/j.compositesb.2024.111526>.
- [39] He QY, Cao SS, Wang YP, Xuan SH, Wang PF, Gong XL. Impact resistance of shear thickening fluid/Kevlar composite treated with shear-stiffening gel. *Compos. Pt. A-Appl. Sci. Manuf.* 2018;106:82–90. <https://doi.org/10.1016/j.compositesa.2017.12.019>.
- [40] Wu LW, Zhao F, Lu ZQ, Lin JH, Jiang Q. Impact energy absorption composites with shear stiffening gel-filled negative Poisson's ratio skeleton by Kirigami method. *Compos Struct* 2022;298:116009. <https://doi.org/10.1016/j.comstruct.2022.116009>.
- [41] Zhao F, Chen H, Gu H, Jiang Q, Lu ZQ, Wu LW. Effect of shear stiffening gel rheology on its Kevlar fabric reinforced composite under low-velocity impact. *J Ind Text* 2022;51:2799S–818S. <https://doi.org/10.1177/15280837221088184>.
- [42] Zhang J, Jiang Q, Zhao F, Zhou KH, Lu ZQ, Liu SK, et al. Cushioning property and structure optimization of double-arrow sandwich composite based on modified genetic algorithm. *J Sandw Struct Mater* 2024;26:1081–6. <https://doi.org/10.1177/10996362241272834>.
- [43] Lam L, Chen W, Hao H, Li Z. Dynamic crushing and energy absorption of bio-inspired shear thickening fluid-filled origami metastructure. *Eng Struct* 2024;299:117122. <https://doi.org/10.1016/j.engstruct.2023.117122>.
- [44] Sheikhi MR, Gürgen S, Li J. Vibration suppression and surface quality enhancement in milling thin-walled structures using shear thickening fluids. *J Manuf Process* 2024;131:2219–29. <https://doi.org/10.1016/j.jmapro.2024.10.038>.
- [45] Zhu JQ, Gu ZP, Liu ZP, Zhong FC, Wu XQ, Huang CG. Silicone rubber matrix composites with shear thickening fluid microcapsules realizing intelligent adaptation to impact loadings. *Compos. Pt. B-Eng.* 2022;247:110312. <https://doi.org/10.1016/j.compositesb.2022.110312>.
- [46] Gürgen S, Sofuoğlu MA. Vibration attenuation of sandwich structures filled with shear thickening fluids. *Compos. Pt. B-Eng.* 2020;186:107831. <https://doi.org/10.1016/j.compositesb.2020.107831>.
- [47] Liu LL, Cai M, Liu X, Zhao ZH, Chen W. Ballistic impact performance of multi-phase STF-impregnated Kevlar fabrics in aero-engine containment. *Thin-Walled Struct* 2020;157:107103. <https://doi.org/10.1016/j.tws.2020.107103>.
- [48] Xie ZH, Liu YY, Liu LL, Feng R, Jiang W, Chen W. Research on the adaptability of STF-Kevlar to ambient temperature under low-velocity impact conditions. *Polym Test* 2024;133:108416. <https://doi.org/10.1016/j.polymertesting.2024.108416>.
- [49] Zhu J, Gu Z, Liu Z, Zhong F, Wu X, Huang C. Silicone rubber matrix composites with shear thickening fluid microcapsules realizing intelligent adaptation to impact loadings. *Compos. Pt. B-Eng.* 2022;247:110312. <https://doi.org/10.1016/j.compositesb.2022.110312>.
- [50] Wei C, Gu Z, Yue J, Liu Z, Mao CY, Zhong F, et al. Shock attenuation of silicone rubber composites with shear thickening fluid. *Int J Mech Sci* 2024;278:109462. <https://doi.org/10.1016/j.ijmecsci.2024.109462>.
- [51] Zhao F, Wu LW, Lu ZQ, Lin JH, Jiang Q. Design of shear thickening fluid/polyurethane foam skeleton sandwich composite based on non-Newtonian fluid solid interaction under low-velocity impact. *Mater Des* 2022;213:110375. <https://doi.org/10.1016/j.matdes.2021.110375>.
- [52] Lu ZQ, Yuan ZS, Chen XG, Qiu JW. Evaluation of ballistic performance of STF impregnated fabrics under high velocity impact. *Compos Struct* 2019;227:111208. <https://doi.org/10.1016/j.comstruct.2019.111208>.
- [53] Hu Q, Lu G, Hameed N, Tse KM. Dynamic compressive behaviour of shear thickening fluid-filled honeycomb. *Int J Mech Sci* 2022;229:107493. <https://doi.org/10.1016/j.ijmecsci.2022.107493>.
- [54] Hu Q, Lu G, Tse KM. Dynamic responses of shear thickening fluid-filled lattice structures. *Int J Impact Eng* 2024;189:104954. <https://doi.org/10.1016/j.ijimpeng.2024.104954>.
- [55] Sun H, Tse KM, Hameed N, Li G. Dynamic compressive behavior of Miura-ori metamaterials filled with shear thickening fluid. *Int J Mech Sci* 2025;288:110006. <https://doi.org/10.1016/j.ijmecsci.2025.110006>.
- [56] Wei LL, Zhao X, Yu Q, Zhu GH. A novel star auxetic honeycomb with enhanced in-plane crushing strength. *Thin-Walled Struct* 2020;149:106623. <https://doi.org/10.1016/j.tws.2020.106623>.
- [57] Wang H, Lu Z, Yang Z, Li X. In-plane dynamic crushing behaviors of a novel auxetic honeycomb with two plateau stress regions. *Int J Mech Sci* 2019;151:746–59. <https://doi.org/10.1016/j.ijmecsci.2018.12.009>.
- [58] Li X, Li Z, Guo Z, Mo Z, Li J. A novel star-shaped honeycomb with enhanced energy absorption. *Compos Struct* 2023;309:116716. <https://doi.org/10.1016/j.comstruct.2023.116716>.
- [59] Hu LL, Luo ZR, Zhang ZY, Lian MK, Huang LS. Mechanical property of re-entrant anti-trichiral honeycombs under large deformation. *Compos. Pt. B-Eng.* 2019;163:107–20. <https://doi.org/10.1016/j.compositesb.2018.11.010>.
- [60] Gu ZP, Wu XQ, Li QM, Yin QY, Huang CG. Dynamic compressive behaviour of sandwich panels with lattice truss core filled by shear thickening fluid. *Int J Impact Eng* 2020;143:103616. <https://doi.org/10.1016/j.ijimpeng.2020.103616>.
- [61] Wu X, Xiao K, Yin Q, Zhong F, Huang C. Experimental study on dynamic compressive behaviour of sandwich panel with shear thickening fluid filled pyramidal lattice truss core. *Int J Mech Sci* 2018;138–139:467–75. <https://doi.org/10.1016/j.ijmecsci.2018.02.029>.
- [62] Gu Z, Wei C, Wu X, Huang C. Laser-induced shock response of shear thickening fluid. *Acta Mech Sin* 2023;39:123118. <https://doi.org/10.1007/s10409-023-23118-x>.
- [63] Ren KR, Yuan WH, Qing H, Peng Y, Xu WT, Jia HB, et al. Dynamic responses of kerosene-filled riveted tanks subjected to hydrodynamic ram caused by ballistic impacts. *Thin-Walled Struct* 2024;197:111337. <https://doi.org/10.1016/j.tws.2023.111337>.
- [64] Ren KR, Miao JT, Qing H, Xu WT, Peng Y, Jia HB, et al. Dynamic responses of riveted fuel containers subjected to oblique impacts. *Thin-Walled Struct* 2025;207:112746. <https://doi.org/10.1016/j.tws.2024.112746>.
- [65] Frutos Martínez JA, Ambriz RR, Nait-Abdelaziz M, Jaramillo D. Impact test behavior of aluminum alloys welded joints: experimental and numerical analysis. *Fatigue Fract. Eng. Mater. Struct.* 2021;44:2119–34. <https://doi.org/10.1111/ffe.13482>.
- [66] van der Naald M, Zhao L, Jackson GL, Jaeger HM. The role of solvent molecular weight in shear thickening and shear jamming. *Soft Matter* 2021;17:3144–52. <https://doi.org/10.1039/d0sm01350a>.
- [67] Luo G, Chai CP, Chen YS, Li L, Xue P. Investigations on the quasi-static/dynamic mechanical properties of 3D printed random honeycombs under in-plane compression. *Thin-Walled Struct* 2023;190:110931. <https://doi.org/10.1016/j.tws.2023.110931>.
- [68] Höning A, Stronge WJ. In-plane dynamic crushing of honeycomb.: Part I: crush band initiation and wave trapping. *Int J Mech Sci* 2002;44:1665–96. [https://doi.org/10.1016/s0020-7403\(02\)00060-7](https://doi.org/10.1016/s0020-7403(02)00060-7).
- [69] Tan PJ, Reid SR, Harrigan JJ, Zou Z, Li S. Dynamic compressive strength properties of aluminium foams. Part II—‘shock’ theory and comparison with experimental data and numerical models. *J. Mech. Phys. Solids* 2005;53:2206–30. <https://doi.org/10.1016/j.jmps.2005.05.003>.
- [70] Jing L, Wang ZH, Zhao LM. An approximate theoretical analysis for clamped cylindrical sandwich shells with metallic foam cores subjected to impulsive loading. *Compos. Pt. B-Eng.* 2014;60:150–7. <https://doi.org/10.1016/j.compositesb.2013.12.047>.
- [71] Nian Y, Wan S, Zhou P, Wang X, Santiago R, Li M. Energy absorption characteristics of functionally graded polymer-based lattice structures filled aluminum tubes under transverse impact loading. *Mater Des* 2021;209:110011. <https://doi.org/10.1016/j.matdes.2021.110011>.
- [72] Lam L, Chen W, Hao H, Li Z, Ha NS. Dynamic crushing performance of bio-inspired sandwich structures with beetle forewing cores. *Int J Impact Eng* 2023;173:104456. <https://doi.org/10.1016/j.ijimpeng.2022.104456>.
- [73] Wu X, Zhong F, Yin Q, Huang C. Dynamic response of shear thickening fluid under laser induced shock. *Appl Phys Lett* 2015;106:071903. <https://doi.org/10.1063/1.4913423>.